

## Article

# Preparation of Laser-Ablated Ag Nanoparticle–MMT Clay-Based Beeswax Antibiofilm Coating

Syed Imdadul Hossain <sup>1,2</sup>, Diellza Bajrami <sup>3</sup>, Maria Chiara Sportelli <sup>1</sup>, Rosaria Anna Picca <sup>1,2</sup>, Annalisa Volpe <sup>4,5,6</sup>, Caterina Gaudiuso <sup>4,5,6</sup>, Antonio Ancona <sup>4,5,6</sup>, Luigi Gentile <sup>1,2</sup>, Gerardo Palazzo <sup>1,2</sup>, Nicoletta Ditaranto <sup>1,2</sup>, Boris Mizaikoff <sup>3,7</sup> and Nicola Cioffi <sup>1,2,\*</sup>

<sup>1</sup> Chemistry Department, University of Bari “Aldo Moro”, Via E. Orabona 4, 70126 Bari, Italy

<sup>2</sup> CSGI (Center for Colloid and Surface Science) c/o, Department of Chemistry, Via Orabona 4, 70125 Bari, Italy

<sup>3</sup> Institute of Analytical and Bioanalytical Chemistry, Ulm University, Albert Einstein-Allee 11, 89081 Ulm, Germany

<sup>4</sup> Physics Department “M. Merlin”, University of Bari “Aldo Moro”, Via E. Orabona 4, 70126 Bari, Italy

<sup>5</sup> Politecnico of Bari, Via E. Orabona 4, 70126 Bari, Italy

<sup>6</sup> Physics Department “M. Merlin”, IFN–CNR (Istituto di Fotonica e Nanotecnologie–Consiglio Nazionale delle Ricerche), Via Amendola 173, 70126 Bari, Italy

<sup>7</sup> Hahn-Schickard Institute for Microanalysis Systems, Sedanstrasse 14, 89077 Ulm, Germany

\* Correspondence: nicola.cioffi@uniba.it

**Abstract:** Unlike other antimicrobial agents, Ag-based composites are stable and currently widely used as broad spectral additives, fighting microbial biofilms and other biological threats. The goal of the present study is to develop a green, multifunctional, and robust antibiofilm water-insoluble coating, inhibiting histamine-producing *Lentilactobacillus parabuchneri* biofilms. Herein, laser-ablated Ag NPs (L-Ag NPs) were incorporated into and onto a montmorillonite (MMT) surface layer with a simple wet chemical method, provided that the electrostatic interaction between L-Ag NPs and MMT clay led to the formation of L-Ag/MMT nanoantimicrobials (NAMs). The use of MMT support can facilitate handling Ag NPs in industrial applications. The Ag/MMT composite was characterized with transmission electron microscopy (TEM) and scanning electron microscopy (SEM), which confirmed the entrapment of L-Ag NPs into MMT clay. The surface chemical composition was assessed with X-ray photoelectron spectroscopy, proving that Ag NPs were in contact with and deposited onto the surface of MMT. The characteristic L-Ag/MMT band was investigated with UV–vis spectroscopy. Following that, the L-Ag/MMT composite was embedded into a biosafe water-insoluble beeswax agent with a spin coating technique. The antimicrobial ion release kinetic profile of the L-Ag/MMT/beeswax coating through an electrothermal atomic absorption spectroscopy (ETAAS) study supported the controlled release of Ag ions, reaching a plateau at  $420 \pm 80$  nM, which is safe from the point of view of Ag toxicity. Microbial biofilm growth inhibition was assessed with real-time in situ Fourier transform infrared attenuated total reflection spectroscopy (FTIR-ATR) in a flow cell assembly over 32 h. The study was further supported by optical density (OD) measurements and SEM on bacteria incubated in the presence of the L-Ag/MMT/beeswax coating.

**Keywords:** antimicrobial; antibiofilms; silver; montmorillonite; beeswax; coating

**Citation:** Hossain, S.I.; Bajrami, D.; Sportelli, M.C.; Picca, R.A.; Volpe, A.; Gaudiuso, C.; Ancona, A.; Gentile, L.; Palazzo, G.; Ditaranto, N.; et al. Preparation of Laser-Ablated Ag Nanoparticle–MMT Clay-Based Beeswax Antibiofilm Coating. *Antibiotics* **2023**, *12*, 194. <https://doi.org/10.3390/antibiotics12020194>

Academic Editor: Marc Maresca

Received: 31 December 2022

Revised: 12 January 2023

Accepted: 15 January 2023

Published: 17 January 2023



**Copyright:** © 2023 by the authors. Licensee MDPI, Basel, Switzerland. This article is an open access article distributed under the terms and conditions of the Creative Commons Attribution (CC BY) license (<https://creativecommons.org/licenses/by/4.0/>).

## 1. Introduction

Antimicrobial resistance (AMR) is a global threat facing humanity. The European Centre for Disease Prevention and Control (ECDC) reported that AMR is a growing concern to public health [1]. The significant impact of AMR on the economy, health, and society includes human disability, severe illness, and longer hospital stays, which require more expensive medicines. The success of medicine in treating infection and major

surgery would be at high risk without the support of effective nanoantimicrobials (NAMs) because, on the one hand, currently available and newly developed antibiotics are not enough to race against AMR; on the other hand, bacteria produce colonies on medical devices and food packaging. Viruses, bacteria, fungi, and parasites have the ability to transfer genes, changing their mechanism of action over time, surviving harsh environments, and becoming so strong that they render antibiotics and antimicrobials ineffective. AMR organisms may be found in people, animals, food, plants, soil, and air [2]. Urgent action and plans are imperative for the sustainable development of antimicrobial materials. A lack of access to effective antimicrobials remains a major issue. For those reasons, extensive research focus should be devoted to developing novel antimicrobial agents. However, challenges still remain, as antimicrobial resistance is continuously occurring globally, and the overuse of antimicrobial agents poses the possibility of increasing antimicrobial resistance. Therefore, the use and concept of AM agents should be optimized. The aim is to design particular synergistic AM agents with the multifunctional activities, ecofriendly material, optimized dose, concentration ion release kinetics, shape, and size of NAMs. Top priority should be given to the development of potential AM agents that can inhibit and eradicate biofilms, which are particularly detrimental to the hospital and industrial sectors, for instance, in food packaging applications. Lactic acid bacteria such as *Lentilactobacillus parabuchneri* are associated with the production of histamine in cheese [3–5]. Biogenic amine (BA) histamine is toxic and responsible for food poisoning. The ingestion of high levels of histamine may cause rashes, headaches, a hypertensive crisis, and gastrointestinal and respiratory problems. Considering its toxicological effects, histamine-forming *L. parabuchneri* strain poses a major risk in the food industry. *L. parabuchneri* strain has the undesirable tendency and strong ability to form biofilms on dairy industry equipment surfaces, further increasing the food toxicity level. *L. parabuchneri* biofilms often develop resistance against disinfecting agents and act as reservoirs of histamine-producing bacteria [3]. The coating of intrinsic antibiofilm materials can reduce *L. parabuchneri* biofilm formation, with great industrial significance in the food-processing industry. Very few studies have been devoted to understand the antimicrobial activity of materials against *L. parabuchneri*. Recently, chitosan and its methylated derivatives have been reported to be active as antimicrobials to inhibit *Lentilactobacillus parabuchneri* biofilms [6]. In another study, an oregano-derived essential oil showed antimicrobial activity against *L. parabuchneri* [7].

The incorporation of metal and metal oxide nanoparticles into different support materials is a promising strategy to produce multifunctional nanocomposites for biosensors, catalysis, surface-enhanced Raman scattering, energy storage, and antimicrobial applications [8–13]. Among various materials, Ag-based nanocomposites have been widely investigated due to their unique properties and wide possibilities for application. The bioactivity of metal nanoparticles such as Cu, Zn, Au, Ti, and Ag is widely known. Among them, Ag NPs showed the most effective antimicrobial activity against a wide range of pathogenic bacteria, yeasts, fungi, and viruses [14]. Ag-based nanocomposites can exert multiple modes of action not only against sensitive bacterial strains, but also against highly resistant bacterial strains. The most commonly known mechanism of action disrupts bacterial metabolic processes, interacts with the DNA, and increases the cytoplasmic membrane permeability [15]. In particular, Ag-based composites were applied as antimicrobial agents in food packaging and biomedicine [16–18]. Various methods, from chemical to hybrid (physical and chemical) synthesis, have been developed to prepare AgNPs. Versatile laser ablation synthesis in solution (LASiS) allows for producing highly stable AgNPs using nontoxic chemicals [19] without requiring precursors and reducing agents. The green and simple LASiS technique produces NPs with unique surface characteristics and without any byproducts [20]. The preparation of NPs on solid support such as montmorillonite (MMT) is highly appreciated, as it can form practically applicable supported particles. MMT nanosheets

allow for preparing multifunctional antimicrobial hybrid nanocomposites with peculiar mechanisms of action, and tunable and enhanced activity against antimicrobial resistant microorganisms. Moreover, the incorporation of colloidal NPs into an MMT matrix could lead to the perspective development of additives for real-life application. The MMT support substrate is highly attractive due to its excellent ion exchange capacity, chemical inertness, natural abundance, cost-effectiveness, nontoxicity, ease of exfoliation to two-dimensional nanosheets, and effortless dispersion in almost all solvents. Furthermore, MMT has the advantage of a lamellar structure and a large surface area, exhibits negative surface charge ( $-63 \pm 11$  mV), and is also biologically inert [21–23]. MMT/metal NP composites exhibit excellent adsorption, rheological, heat-insulator, heat-resistant, and swelling properties [24]. An appealing property of MMT substrates is the propensity to absorb a variety of compounds on their surface. The addition of beeswax into MMT-supported NPs could allow for the controlled release of antimicrobial ions. Beeswax contains more than 300 components: it is a mixture of hydrocarbons, free fatty acids, esters of fatty acids and fatty alcohol, diesters, and exogenous substances [25]. The diversity of this chemical composition gives an additional advantage as an antimicrobial agent, result in it being beneficial for antibiofilm application. The combination of many active ingredients and their presence in various proportions prevent bacterial resistance [26]. Beeswax possesses good antimicrobial activity against a wide range of pathogenic bacteria. Beeswax is commonly used in the cosmetic, food, and pharmaceutical sectors, including for the treatment of burns, wounds, bruises, and fractures [27]. It is considered to be one of the essential hydrophobic materials to reduce moisture permeability [28]. A beeswax surface coating results in a drastic decrease in water vapor penetration, whereas its effects on mechanical properties are generally irrelevant [29]. This property could be beneficial in controlling or slowing down the release of antimicrobial ions for long-term effects. The preparation and extensive analytical characterization of active NAMs play important roles in understanding their mechanism of action and overcoming toxicity issues. Long-term stability and cost-effectiveness can be improved in this way, too. Attenuated total reflection Fourier-transform infrared (ATR-FTIR) spectroscopy can be used for the in situ and real-time monitoring of early-stage biofilm formation with molecular specificity and metabolomic changes [30–32]. One of the major components in biofilms, the extracellular polymeric substance (EPS), plays an important role in biofilm formation, which can be monitored in real time [33].

In the present work, hybrid (physical and chemical) routes are adapted to prepare L-Ag/MMT composites with detailed analytical characterization. Laser-ablated Ag NPs were impregnated into refined MMT (L-Ag/MMT) with a simple wet chemical method using 2-propanol as dispersing solvent. Further, an L-Ag/MMT nanocomposite was introduced into beeswax to develop water-insoluble antimicrobial coatings. The inhibition of biofilm formation by the L-Ag/MMT/beeswax coating provides a strategy to reduce the contamination of food-processing equipment to prevent the spoilage of cheese due to histamine-producing species.

## 2. Results and Discussion

### 2.1. Characterization of L-Ag/MMT and L-Ag/MMT/Beeswax

AgNPs were obtained with ns-pulsed laser ablation in pure isopropanol. The average colloidal concentration was equal to  $0.08 \pm 0.01$  g/L. A TEM micrograph was acquired for L-Ag NPs. AgNPs showed a spherical morphology (Supplementary Materials Figure S1a–c) and an average size diameter of  $10 \pm 3$  nm (Figure S1d). A typical TEM micrograph of the refined MMT and L-Ag/MMT nanocomposite can be seen in Figure 1a,b, respectively. TEM images confirmed the presence of spheroidal AgNPs entrapped into the surface layer of the MMT matrix. Ag NPs were well-dispersed on the MMT matrix without aggregation. A typical SEM image showed AgNPs on the surface of the MMT structures (Figure 1c).

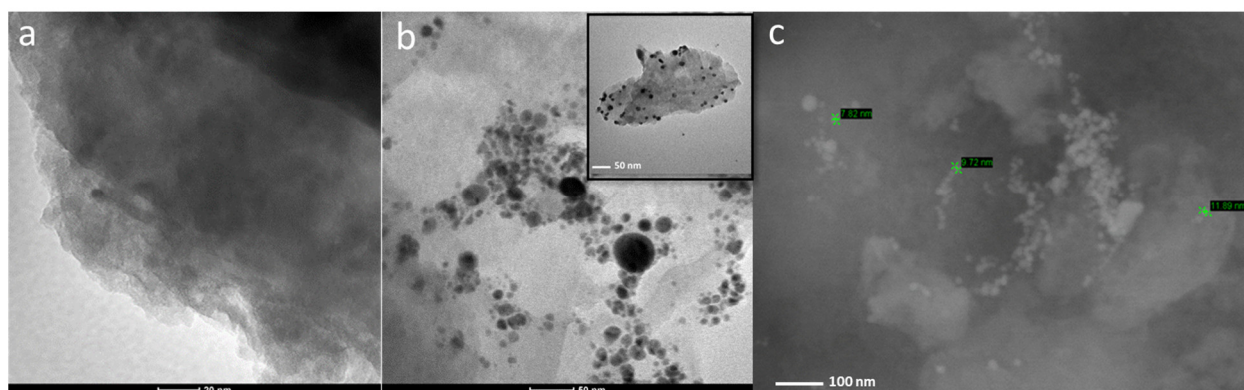


**Figure 1.** TEM images of (a) MMT and (b) L-Ag/MMT; SEM images of (c) L-Ag/MMT.

UV–vis spectra of MMT, L- AgNPs, and L-Ag/MMT can be seen in Figure 2. As expected, MMT displayed a characteristic broad band at 270–280 nm [34], L-Ag showed a surface plasmon resonance (SPR) peak at  $400 \pm 4$  nm. In the case of L-Ag/MMT, the SPR of Ag NPs was observed at  $418 \pm 4$  nm. L-Ag/MMT showed more intense absorption than that of bare MMT and L-AgNPs in the 240 to 450 nm range. Additionally, a shift towards higher wavelengths was observed that was probably associated with the plasmonic behavior of the interaction of small AgNPs with MMT particles [35–38].

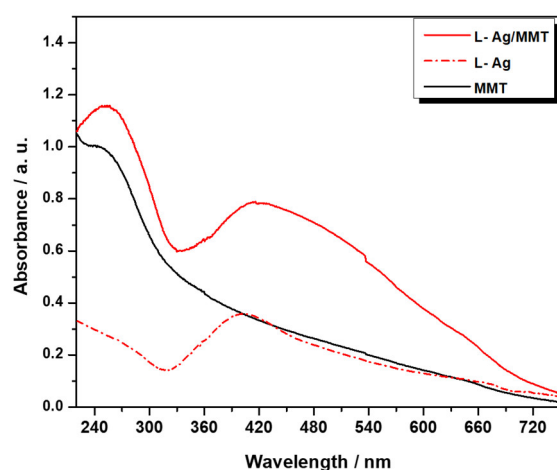


**Figure 2.** UV–vis absorption spectra of MMT, L-Ag, and L-Ag/MMT.

XPS characterization was carried out to confirm the loading of L-Ag NPs into the MMT matrix. Table 1 presents the typical surface compositions of L-Ag NPs, L-Ag/MMT, and refined MMT samples, demonstrating that silver was detected in the L-Ag/MMT nanocomposite. The results of L-Ag NP characterization were in agreement with those in our previous studies, conducted on Ag NPs prepared via laser ablation in isopropanol, in terms of both elemental content and silver speciation [19]. The Ag surface composition was affected by the massive presence of organic matter coming from the degradation of IPA during LASiS, and this is not surprising on the basis of the literature [19]. Despite the very low amount of metal in the final composite, it had a very good antimicrobial and antibiofilm efficacy (*vide infra*). A more detailed analysis was performed on L-Ag/MMT samples to evaluate if any change in silver speciation had occurred in the nanocomposite. The Ag3d high-resolution region and AgMNN Auger spectrum are presented in Figure 3a,b, respectively. The complex Auger signal was curve-fit according to the literature; more details on the component attributions were reported by Bera et al. [39]. The Ag3d<sub>5/2</sub> photoelectronic peak centered at  $368.3 \pm 0.2$  eV (Figure 3a) was compatible with Ag(0) [40].

However, to corroborate this assumption, modified Auger parameter  $\alpha'$  was calculated by summing  $\text{BEAg}3d_{5/2}$  and  $\text{KEAgM}_{4.5}\text{N}_{45}\text{N}_{45}$  (357.8 eV, dashed red line in Figure 3b), giving a value of  $726.1 \pm 0.4$  eV, which is undoubtedly ascribed to elemental silver in the MMT matrix [39].

**Table 1.** Typical surface chemical composition for L-Ag NPs, L-Ag/MMT, and MMT. Errors are expressed as standard deviation on three analysis points.

Samples	At%								
	C	O	Na	Mg	Al	Si	Fe	S	Ag
L-Ag	$92.6 \pm 0.8$	$7.1 \pm 0.7$	/	/	/	/	/	/	$0.3 \pm 0.1$
L-Ag/MMT	$16 \pm 5$	$55 \pm 7$	$0.4 \pm 0.2$	$1.0 \pm 0.2$	$7.8 \pm 1.8$	$17.7 \pm 2.2$	$0.5 \pm 0.2$	$0.5 \pm 0.2$	$1.1 \pm 0.3$
MMT	$26.4 \pm 1.6$	$52.6 \pm 0.6$	/	$0.6 \pm 0.1$	$3.0 \pm 0.2$	$17.0 \pm 0.7$	$0.4 \pm 0.2$	/	/

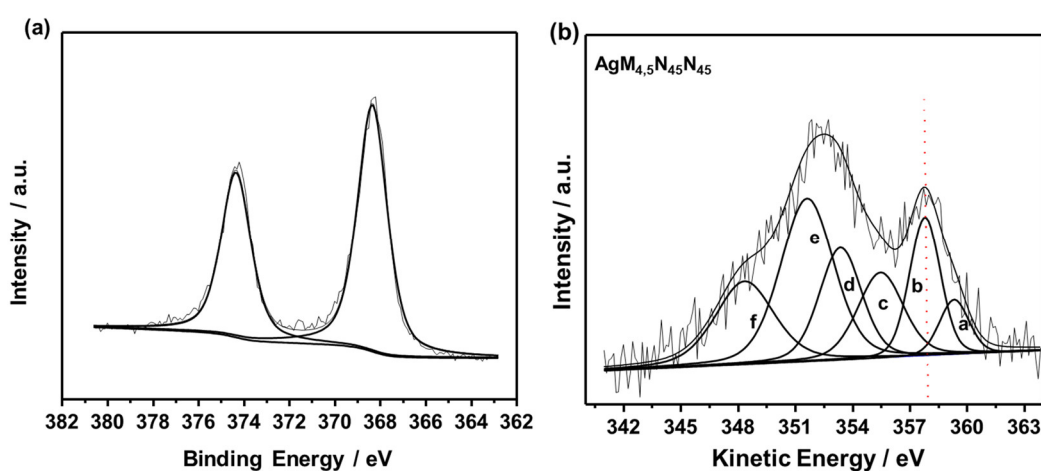


**Figure 3.** (a)  $\text{Ag}3d$  XP and (b)  $\text{AgM}_{4.5}\text{N}_{45}\text{N}_{45}$  Auger spectra of L-Ag/MMT.

The morphological characterization of beeswax and L-Ag/MMT/beeswax-coated silicon wafers was investigated with SEM. The surface of the silicon wafer was covered with a layer of beeswax film with a few wrinkles, as shown in Figure 4a,b. At higher SEM magnification in the L-Ag/MMT/beeswax sample, the beeswax structure was seen to hold MMT-supported Ag NPs (Figure 4c,d).

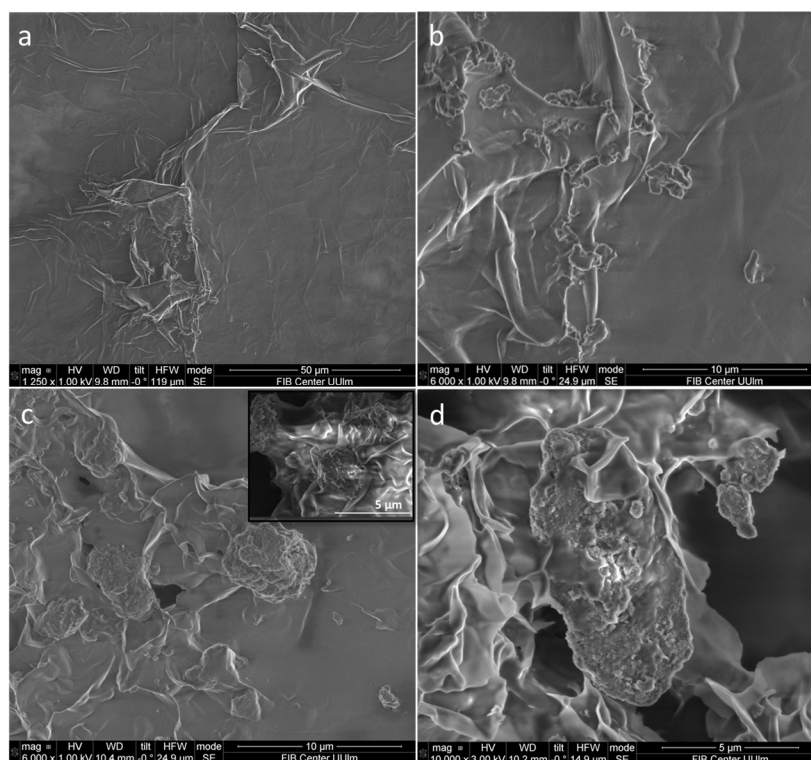


Figure 4. SEM images of (a,b) beeswax and (c,d) L-Ag/MMT/beeswax on silicon substrate.

## 2.2. Kinetics of Silver Release

The silver ion release kinetics was studied on Ag/MMT/beeswax. Experimental points were curve-fitted with a first-order kinetic curve with a rate constant equal to  $17 \pm 6 \text{ h}^{-1}$ .  $\text{Ag}^+$  concentration in the contact solution increased as a function of time, reaching a plateau at about  $45 \pm 9 \text{ ppb}$ , as shown in Figure 5. These results indicate that there was a controlled release of  $\text{Ag}^+$  ions. The measured silver concentration is expected to exert long-term biostatic activity. In this context, a very low amount of Ag NPs in the final composite showed good antimicrobial and antibiofilm efficacy. This limited the final cost of the nanocomposite and reduced toxicological risks associated with the use of silver as bioactive material.

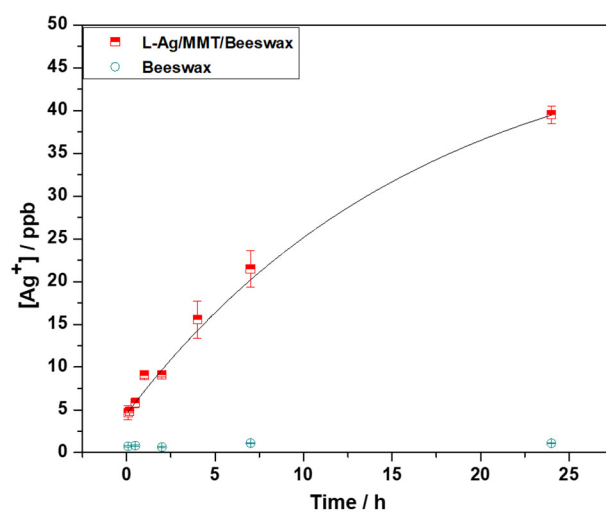


Figure 5. Ion release kinetics of L-Ag/MMT/beeswax coating.



### 2.3. Biofilm Inhibition Efficiency on the Coated ZnSe Surface

Antiadhesive and antibiofilm L-Ag/MMT/beeswax nonantimicrobial coatings for eradicating these biofilms are based on the prevention of biofilm formation in quorum sensing (QS) inhibition via intercellular signaling mechanisms [41]. The biofilm inhibition pathway of AgNPs is attributed to interactions with the microbial membrane of bacteria and the disruption of membrane permeability [42]. AgNPs damage the bacterial outer membrane by inducing pits and gaps in the microbial membrane, and fragment the cell [43]. Microbial cells, in the outer surface of their membrane, carry negative charges resulting in electrostatic interaction between the antimicrobial L-Ag/MMT and cell membrane, and leading to the inhibition of *L. parabuchneri* growth. The prominent contribution is the incorporation of Ag into MMT as a solid supporting material for producing multifunctional hybrid nanocomposites, favoring strong ion exchange capacity between the nonantimicrobial and bacterial communities of cells. The ability of MMT to absorb compounds on its surface allows for its hydrophobic region and protective properties to merge of beeswax [44]. An investigation of the inhibitory mechanism via in situ FTIR-ATR spectroscopy provides a clear overview of the antibiofilm action of L-Ag/MMT/beeswax nanocomposite.

The nondestructive FTIR-ATR spectroscopy technique allows for a more comprehensive characterization of microbial biofilms in order to understand the fundamental mechanisms involved in bacterial adhesion and attachment [45]. Despite the complexity of IR spectra, it is evident that the contribution of bacterial biofilm components corresponds to stretching and bending vibrations including symmetric and asymmetric modes, respectively [46]. The approach used here allows for the in situ monitoring of *L. parabuchneri* biofilm formation and inhibition [47].

On the bare surface of a ZnSe crystal, the initial biofilm attachment was manifested with a constant increase in the bands attributable to biofilm constituents. It was instantly seen that all bands related to amides I and II, nucleic acids, and extracellular polymeric substance (EPS) increased significantly over time. The constantly low increment of amide III and nucleic acid level indicates the amide bond in membrane proteins, fatty acid chains, and ribosomes as bacterial cell components assigned to these prominent band vibrations [48]. Figure 6 shows the spectra of *L. parabuchneri* biofilms on bare and L-Ag/MMT/beeswax-modified waveguides. During 32 h of monitoring on the bare crystal, the bands related to biofilms significantly increased over time, indicating the continuous coverage of the crystal surface with microbial biomass. In the case of the patterned crystal, the intensity of all the bands related to biofilms (amides I–III, lactate, nucleic acid, EPS) [49] slightly decreased over time. The stress generated from the compact and homogeneous nonantimicrobial coating slowed down biofilm proliferation. Particularly, the bands associated with amide I (1700–1616  $\text{cm}^{-1}$ ), amide II (1578–1476  $\text{cm}^{-1}$ ), lactate production (1465–1293  $\text{cm}^{-1}$ ), amide III (1350–1200  $\text{cm}^{-1}$ ), nucleic acid (1280–1175  $\text{cm}^{-1}$ ), and extracellular polymeric substance (EPS)(1038–989  $\text{cm}^{-1}$ ) became visibly lower, indicating the constant detachment of microbial biomass on the surface of the ZnSe waveguide.

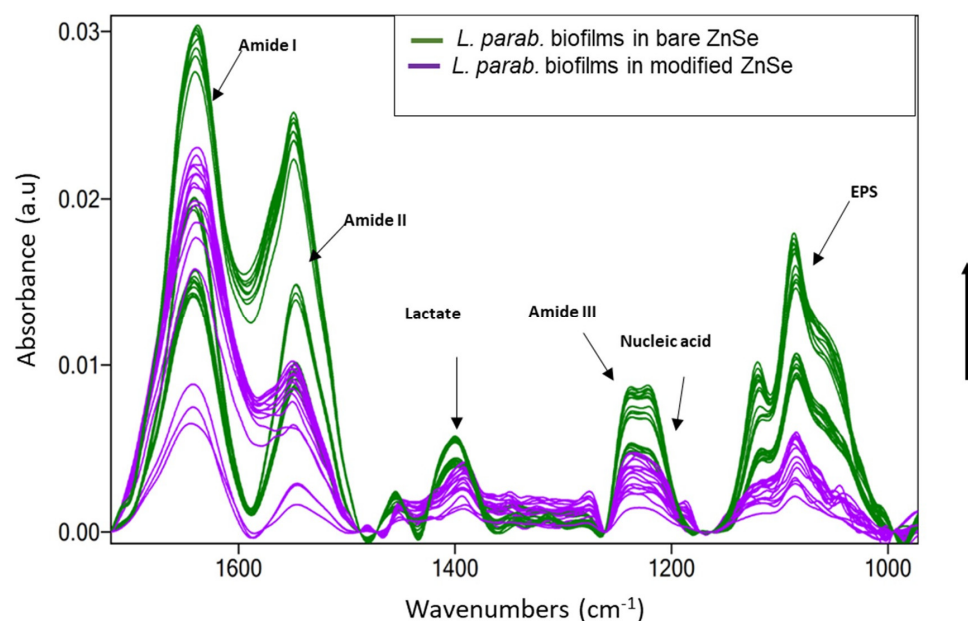


**Figure 6.** Infrared ATR spectra of 32 h old *L. parabuchneri* biofilms assigned by fluctuations in amides I–III, lactate, nucleic acid, and EPS as time-varying absorbance bands monitored (green line) on a bare ZnSe crystal and (purple line) on an L-Ag/MMT/beeswax modified ZnSe crystal at inactive sensing regions. The arrow in the y axis indicates the time evolution from 0 h (at the bottom) until 32 h (at the top).

In Figure 7a, the integrated areas of the amide I and II bands are depicted for biofilms formed over a period of 32 h. It is immediately evident that a recurrent change in absorbance intensity was observed as a consistent decrease over hours of monitoring the flow system of the modified waveguide. This inhibition ability is indicative of the biostatic action of the L-Ag/MMT/beeswax composite film despite the tendency to reach zero. The amide I band, expressed in the infrared vibrations of  $\nu\text{C}=\text{O}$  coupled with  $\text{N}-\text{H} \delta\text{H}_2\text{O}$ , was related to cell membrane constituents [50]. The amide II band, assigned to  $\delta\text{N}-\text{H}$  coupled with  $\text{C}-\text{N}$  vibrations, indicates proteins within the cytoplasm, flagella, pili, and membranes. Silver ions released by the L-Ag/MMT/beeswax coating could penetrate the cell membrane and interact with cell organelles, consequently leading to the disorganization of cell functionality [51]. This is the main reason for the constant decrement of absorbance intensity observed for amide I, and the same continuous decrease in amide II with much higher efficiency. It is apparent that there was less biofilm attached to the crystal surface. *Lentilactobacillus parabuchneri* is responsible for the contamination and food spoilage of cheese and other dairy products [52–54]. Being a basic biogenic amino compound with a flexible ethylamine side-chain moiety, histamine is released during the biofilm formation of *L. parabuchneri* [4], which is why controlling the amide range is important for tracing the histamine-producing biofilms of this specific bacterium [4,55]. The integrated peak values of amide III and nucleic acid shown in Figure 7b confirmed the gradual decrease in both nucleoid cell components after the direct contact of the bacterial cells with the antimicrobial coating. The different secondary protein structures of cell membranes and nucleoids reflect a greater spectral difference in the amide III range than that in amide I [56].

Extracellular polymeric substances (EPSs) are major biomolecules in microbial aggregates kept together in a three-dimensional matrix [57]. EPS are the main indicator of biofilm formation. Polysaccharides, phospholipids, phosphodiester, etc. are the fraction of the EPS matrix that maintains the multicellular microbial communities [58,59]. The combination of bands revealing the EPS presence of biofilm matrix [30] consists of  $\nu\text{C}-\text{O}-\text{C}$ ,  $\nu\text{C}-\text{O}$ ,  $\nu\text{C}-\text{C}$ ,  $\delta\text{C}-\text{O}-\text{C}$ ,  $\nu\text{C}-\text{OH}$ ,  $\nu\text{C}-\text{O}$ ,  $\nu\text{C}-\text{O}-\text{C}$ , vibrational groups ( $1138\text{--}989\text{ cm}^{-1}$ ). The evaluation of EPS bands as a function of time for a bare and modified crystal is shown in



Figure 7c. The intensity of the EPS band increased during *L. parabuchneri* biofilm formation on the bare crystal, reaching the maximum in about 8 h. EPS traces confirmed lactobacillus biofilm growth within the first hours of monitoring, similarly to any type of bacteria [60]. The nutrient gradient was increased over time with the switched inoculum into the FTIR-ATR flow cell, making space for a slight increase in the EPS band, while proteins in the bottom layer of biofilms spread horizontally [61]. In the case of the inactive spot experiment, the biofilms formed during exposure to L-Ag/MMT/beeswax coating, and a slower crystal coverage occurred. This is associated with the fact that less biofilm was attached to the surface due to the antimicrobial L-Ag/MMT/beeswax film. On that basis, all molecular bands after 2 h of monitoring reached almost zero, indicating an early stage of biofilm formation, except for amide III band, which was below zero. The efficient antibiofilm activity was related to biofilm death and the lysis process [62]. The antibacterial action was investigated through the evaluation of nucleic acid phosphate groups ( $\sim 1220\text{ cm}^{-1}$ ) among other bands, related primarily to the metabolic activity of bacteria inside the biofilm [63,64]. The increment of asymmetric stretching  $\text{PO}_2^-$  implied enhanced metabolomic cell activity of the *L. parabuchneri* biofilms close to the ZnSe waveguide surface (Figure 7d). The meager shift at 15–20 h of monitoring was attributed to the loss of proteins due to a lack of nutrients until the continuous inoculation of fresh MRS media into the flow FTIR-ATR system [24]. Then, for the modified crystal by antimicrobial film, a uniform decrease appeared after 10 h due to the stress induced by the nanomaterial film, along with a slow decrease in the signals for the continuous 32 h of monitoring, indicating that no colonization occurred on the entire ZnSe surface.

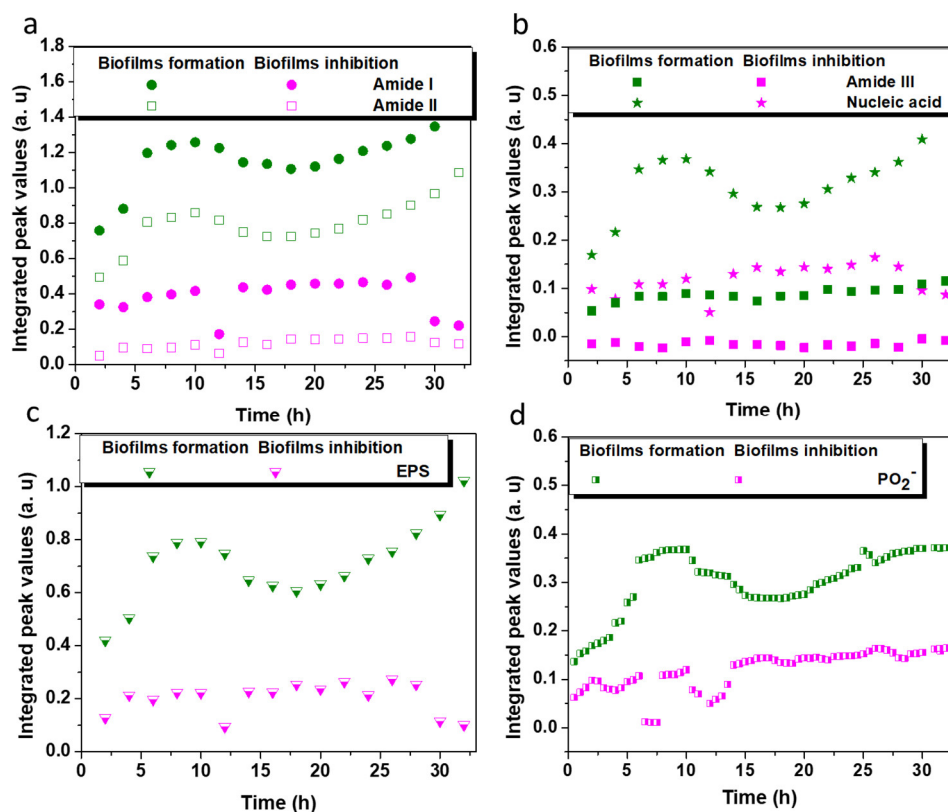


**Figure 7.** Integrated peak values (IPV) as a function of time for the *L. parabuchneri* biofilm formation on bare crystal (olive line) and biofilm inhibition on top of L-Ag/MMT/beeswax modified crystal (magenta line) for (a) amides I and II, (b) amide III and nucleic acid, (c) EPS matrices, and (d)  $\nu_{\text{as}}\text{PO}_2^-$  band obtained with in situ ATR-FTIR spectroscopy.

The decrement in biofilm microbial density was also associated with the sharp decrease in the intensity of the carbohydrates, protein vibrations  $\nu_{\text{C-O}}$ ,  $\nu_{\text{C-OH}}$  ( $1124\text{ cm}^{-1}$ ),

phosphodiester, phospholipid band  $\nu\text{PO}_2^-$  ( $1086\text{ cm}^{-1}$ ) as a correlation of membrane cell wall, and the very important polysaccharide functional groups,  $\nu\text{O-H}$  coupled with  $\delta\text{C-O}$  and  $\nu\text{C-O-C}$ ,  $\nu\text{P-O-C}$  ( $1038\text{ cm}^{-1}$ ) from peptidoglycan [65], capsule and cell walls as cellular components (Table S1). Fluctuations in the EPS and phosphate bands with a decreasing trend were assigned to reduced cell activity [66] due to the distraction mechanisms coming from the nano-anti-microbial coating. The crystal bacterial colonization was impeded by the silver ions in the flow cell that were released into the system of biofilm monitoring. Furthermore, this permitted the decoupling of antibacterial effects that had been caused by  $\text{Ag}^+$  from the cellular stress induced by the direct contact of Ag NPs and *L. parabuchneri* bacteria via the oxidation of surface silver atoms from the dissolved oxidants in the cytoplasm of bacterial cells [51]. Regardless of the high impact from the beeswax hydrophobicity that influenced the late microbial attachment, the main interaction mechanisms of biofilm growth control were determined via the stress coming from nonantimicrobial coating. The molecular mechanisms of the antimicrobial action associated with AgNP-based coatings are necessary for the rational design of AgNPs for food industry packing and pharmaceutical formulations.

#### 2.4. Optical Density Measurement and Microscopy on *L. parabuchneri* Biofilms

The OD of the bacterial suspension was measured after treatment for 24 h using the developed coating (Figure S2). A substantial decrease in OD values was observed for the L-Ag/MMT/beeswax coating, which indicated the potential inhibition of biofilm growth on the coated surface. In the presence of the beeswax coatings used as controls, almost the same OD values as those of uncoated silicon wafer were observed.

The silicon surface is easily colonized by bacterial cells. Hence, bacterial biofilm colonization was observed on the pristine silicon substrate and L-Ag/MMT/beeswax-coated silicon substrate via SEM analyses. Figure 8a shows *L. parabuchneri* after 24 h incubation on bare silicon, which clearly reveals that most of the bacterial cells were embedded in small colonies. The development of *L. parabuchneri* can be defined as structural organization showing a dense network of rod-shaped *L. parabuchneri* cells. The L-Ag/MMT/beeswax-modified surface significantly inhibited the formation of colonies, as can be seen in Figure 8b. The antimicrobial-coated surface could substantially reduce the cell metabolism rate, causing changes in the bacterial colony structure [67]. Further, antimicrobial influence could destroy the network of EPS matrices and disintegrate the biofilms into individual cells [68]. A very low number of individual cells were observed on the L-Ag/MMT/beeswax-coated surface, as shown in detail in Figure 8c. This could have been due to the intrinsic hydrophobic nature of the coating [28]. In addition, the intrinsic antimicrobial activity of silver ions and their controlled release could be what hindered the formation of bacterial communities.

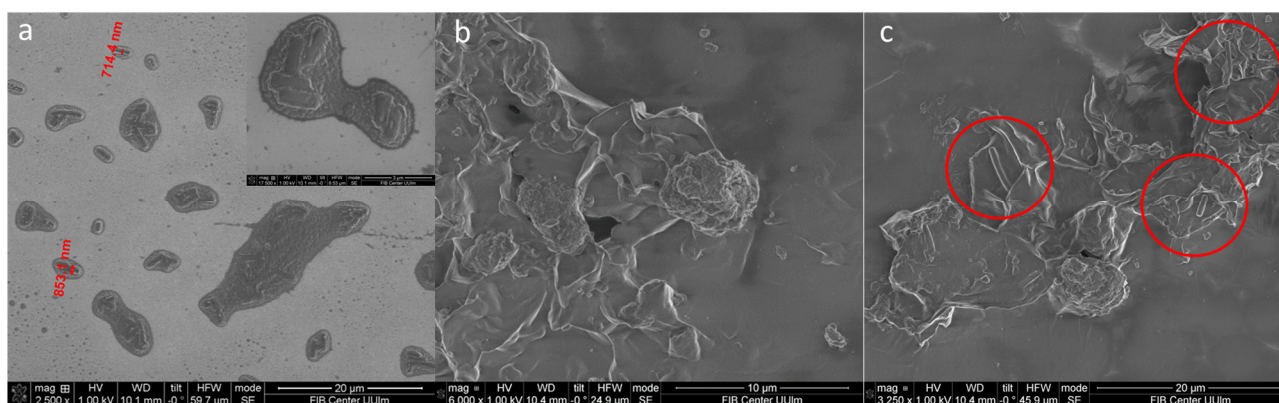


**Figure 8.** SEM images of (a) silicon substrate and (b,c) L-Ag/MMT/beeswax coating incubated in *L. parabuchneri* bacterial suspension for 24 h.

### 3. Materials and Methods

#### 3.1. Materials

Silver sheets (99.99% purity, diameter: 10 mm; nominal thickness: 1 mm) were purchased from Good Fellow Ltd. (Cambridge, UK). Isopropanol (IPA, >99.9%, HPLC grade), ethanol (EtOH, absolute, ACS reagent), HNO<sub>3</sub> (67%, Trace-SELECT® Ultra, for ultratrace analysis), NaCl (Trace-SELECT® Ultra, ≥99.999%, for ultratrace analysis), Cu grids (Agar Scientific, Stansted, UK), carbon-coated, 300-mesh were used for the preparation of TEM samples. Montmorillonite (K10, powder) was bought from Sigma Aldrich, and beeswax (bleached, white) from Acros Organics.

#### 3.2. Preparation of L-Ag NPs, L-Ag/MMT Nanocomposite, and L-Ag/MMT/Beeswax Coating

The synthetic steps from L-Ag NPs and L-Ag/MMT composite towards the final water-insoluble hard L-Ag/MMT/beeswax coating are depicted. First, L-Ag NPs were prepared following a previously published work [19]. In brief, the LASiS experimental setup consisted of a nanosecond Q-Switched Nd:YAG Laser (Quantel-BRIO) operating at a fundamental wavelength of 1064 nm with a pulse frequency of 20 Hz, a pulse energy of 46.5 mJ, and a nominal pulse duration of 4 ns. The Ag target, after mechanical polishing with wet SiC grinding paper and sonication for 15 min in IPA, was fixed to the wall of a 35 × 25 × 30 mm<sup>3</sup> vessel filled with 10 mL of IPA. A yield of 0.08 mg/mL of Ag NPs in IPA was calculated for 20 min of ablation.

Following that, L-Ag/MMT was prepared by simply mixing L-Ag colloids and MMT. It was necessary to perform washing and refining steps to make the MMT matrix suitable for the accommodation of NPs into/onto its layer/surface. To this aim, MMT (K10) was dried overnight at 80 °C. After that, dried MMT was ground using a mortar and pestle, and washed in deionized water at a ratio of 50 mg MMT:1 mL water for 30 min. Larger particles were removed with sedimentation; the upper portion of the suspension was centrifuged, and subsequently dried and ground to obtain refined MMT. Refined MMT was dispersed in IPA and subsequently previously prepared L-AgNPs/IPA solution was added to the MMT/IPA dispersion at an Ag:MMT ratio of 1:37. The mixture was then stirred at room temperature for 60 min until well-dispersed MMT in IPA had been acquired. The mixture was lastly centrifuged at 5000 rpm for 5 min to collect the L-Ag/MMT composite. The sample was washed 3 times with 99.9% IPA.

L-Ag/MMT 0.5%w/w composites were mixed with 10 g/L beeswax in IPA under stirring at 60 °C for 10 min. Then, 500 µL of this suspension was deposited onto 2 × 2 cm<sup>2</sup> glass slides, Si wafers, or aluminum foil via spin coating with a rotation program of 2500 rpm for 20 s

#### 3.3. TEM and SEM Morphological Characterization

TEM analysis was performed using an FEI Tecnai 12 instrument (120 kV; filament: LaB<sub>6</sub>). Samples were drop-cast onto carbon grids (300 mesh, Agar Scientific, Stansted, UK) at a volume of 2 to 3 µL for each sample. Size distribution analysis was performed with ImageJ software. The morphology of the L-Ag/MMT composite was evaluated with FE-SEM model Sigma Zeiss (Jena, Germany), 10 kV acceleration voltage, using a 30 nm aperture and inlens detector. The coatings before and after incubation with the bacteria were assessed via SEM measurements with a dual-beam FIB/SEM system (Quanta 3D FEG, FEI Company, Eindhoven, The Netherlands).

#### 3.4. XPS and UV-Vis Characterization

L-Ag NPs and L-Ag/MMT composites were analyzed with a PHI 5000 Versa Probe II Scanning XPS Microprobe spectrometer (ULVAC-PHI Inc., Kanagawa, Japan). The measurements were performed using a monochromatized Al K $\alpha$  source (X-ray spot 200 µm) at power of 50.3 W. Wide scans and detailed spectra were acquired in fixed analyzer transmission (FAT) mode with pass energies of 117.40 and 46.95 eV, respectively. An electron

gun was used for charge compensation (1.0 V, 20.0  $\mu$ A). The binding energy (BE) scale was calibrated by fixing the aliphatic component of the C1s signal (BE = 284.8  $\pm$  0.1 eV) as the reference. Data processing was performed by using MultiPak software v. 9.9.0.8. The absorption spectra of L-Ag, L-Ag/MMT, and MMT were measured using UV-vis spectroscopy (Shimadzu UV-1601, Duisburg, Germany), operating the spectrometer in the 220 and 800 nm range in quartz Suprasil<sup>®</sup> cuvettes from Hellma Analytics (Müllheim, Germany). A total of 3.5 mg/mL of L-Ag/MMT was used for the UV-vis experiment.

### 3.5. Determination of Silver Release

The kinetics of silver released from the L-Ag/MMT/beeswax coating into aqueous contact solutions was determined through ETAAS. Glass slides were laid onto a small Petri dish and covered with 3 mL of the contact solution. The contact solution was a 1:1 mixture of phosphate buffer (pH 6.8, ionic strength 0.1) and 0.85% *w/w* NaCl. Contact solution aliquots were mineralized with 0.5% HNO<sub>3</sub> and then analyzed. The release experiments were conducted at a controlled temperature (21  $\pm$  2°C) in an air-conditioned room and at controlled environmental humidity (75  $\pm$  2%), thus mimicking real-life conditions.

### 3.6. Bacterial Growth and Culture Conditions

The DSMZ 5987 strain of lactic acid bacterium *Lentilactobacillus parabuchneri* was obtained from the Leibniz Institute, German Collection of Microorganisms and Cell Cultures (DSMZ), Niedersachsen, Germany. The bacterial cells were maintained in Man de Rogosa Sharpe (MRS) broth in a microaerophilic environment during incubation at 37 °C for 24 h. At the end of the exponential growth phase, the optical density (OD-600) of the bacterial solutions was monitored using a UV-vis spectrophotometer (Specord S600, Analytik Jena AG, Germany). Cells were resuspended in fresh MRS medium to reach OD<sub>600</sub> = 0.7 ready for in situ IR spectroscopy. The strain was isolated at -80 °C in MRS with 10% (*w/v*) sterile glycerol.

### 3.7. Modification of ZnSe Waveguide in Inactive Spots

FTIR-ATR spectroscopy was used to evaluate the biofilm inhibition ability of the L-Ag/MMT/beeswax coating. To conduct this experiment, we determined the evanescent wave regions along the surface of a 72  $\times$  10  $\times$  6 mm trapezoidal horizontal ATR crystal (45° in coupling facet, six reflections) produced from ZnSe. The crystal was mounted onto a customized horizontal flow cell with the top plate removed, facilitating the deposition of absorbing blended materials droplets at the crystal surface. The ZnSe crystal was modified in a way that only IR inactive regions of the waveguide were covered by the deposited L-Ag/MMT/beeswax blend. This approach allowed for simplifying the system, limiting bioactivity mechanisms only to the biofilm exposure towards metal ions. Previous studies showed the localization of IR-active sensing regions [64,69], helping to determine IR-inactive areas along the crystal surface; thus, we avoid infrared signals being convoluted with absorption intensity that might come from the composite film. The active spots were able to be attracted by the sampled biofilms as a consequence of exposure only to the Ag<sup>+</sup> ions released by the neighboring regions (3 mm spots of nanoantimicrobials, 0.5 mm thickness). In this regard, two experiments were carried out: (1) modified ZnSe areas in the inactive sensing regions exactly between the internal reflections of the propagating IR radiation, and (2) the bare ZnSe crystal without any pattern on top of it for the normal in situ monitoring of *Lentilactobacillus parabuchneri* biofilm formation.

### 3.8. In Situ FTIR-ATR Spectroscopic Strategy as a Biofilm Inhibition Study

The flow system assembly designed for real-time IR measurements consisted of a flow cell setup connected to the FTIR-ATR multireflection compartment of the Tensor II infrared spectrometer (Bruker Optics, Etlingen, Germany) and a peristaltic pump (Watson Marlow Series 400, Cornwall, UK) with silicon tubing. The spectrophotometer was

equipped with a DTGS detector and a six-reflection ZnSe crystal. The flow cell was mounted into the sample chamber of the infrared spectrometer. Prior to the in situ measurements, the crystal was cleaned in a UV light chamber using intense ultraviolet light. Afterwards, the mounted cell was cleaned with ethanol and rinsed with sterilized water for half an hour. The MRS conditioning film was recorded as a background spectrum for the subsequent *L. parabuchneri* biofilms to minimize water interference [30]. The sterilized MRS medium was flushed in the system for 3 h with a delay of 5 min between measurements at a flow rate of 0.7 mL/min, which resulted in a residence time within the flow cell of ~150 s. After recording the conditioning film background, the MRS media were replaced with a bacterial solution (OD-600 = 0.7) for 2 h at a 0.7 mL/min flow rate with 10 min delay between measurements. This period was optimized on the basis of the required time for initiating the attachment of *Lentilactobacillus parabuchneri* biofilms at the ZnSe waveguide. After 2 h of initial attachment of *L. parabuchneri*, a sterile MRS medium (52 g/L) was pumped again through the FTIR-ATR assembly cell for 20–24 h at a 0.5 mL/min flow rate. A fresh MRS solution medium washed out the free cells that had not been attached and delivered nutrients for the microorganisms. The spectra were recorded at 2 cm<sup>-1</sup> resolution with 100 averaged spectra and in the infrared region of 4000–400 cm<sup>-1</sup> (1700–989 cm<sup>-1</sup> region of interest). Data acquisition was realized with Bruker OPUS™ 8.1 software. Spectra were all converted into Excel datasets using Essential FTIR software (Operant LLC, Madison, WI, USA), and elaborated in the OriginLab software package (OriginLab Corp., Northampton, MA, USA). The IR spectra of the *L. parabuchneri* biofilms were recorded at 22 ± 1 °C in an air-conditioned room. The plotting of integrated peak values (IPVs) was calculated from FTIR on the basis of six spectral regions: amide I (1700–1616 cm<sup>-1</sup>), amide II (1578–1476 cm<sup>-1</sup>), amide III (1350–1200 cm<sup>-1</sup>), nucleic acid (1280–1175 cm<sup>-1</sup>), EPS (1138–989 cm<sup>-1</sup>), and ν<sub>as</sub> PO<sub>2</sub><sup>-</sup> band at 1086 cm<sup>-1</sup> vs. time. The observed bands associated with the molecular components related to the *L. parabuchneri* biofilms showed the progression of the IR signature, which frequently changed as a function of time [70].

### 3.9. Biofilms Grown on Silicon Wafer

We immersed 1 × 1 cm<sup>2</sup> coated silicon wafers in 15 mL of MRS and 150 µL of bacterial suspension (OD = 0.7), and they were incubated for 24 h at 37 °C. Following that, staining was fixed in 2.5% glutaraldehyde and dehydrated with a graded series of acetone solutions (50–100%). After drying, the samples were subjected to SEM analyses.

## 4. Conclusions

In this contribution, a water-insoluble L-Ag/MMT/beeswax antibiofilm coating was developed. MMT was used to support the laser-ablated AgNPs; L-Ag/MMT was then dispersed into beeswax for the controlled release of antimicrobial ions. A microscopic study confirmed the decoration of MMT with spherical AgNPs embedded into beeswax films. UV-vis spectroscopy indicated evidence of the complexation of metal AgNPs with the MMT supporter. XPS characterization provided a detailed surface chemical speciation of the L-Ag/MMT composite, including information regarding Ag chemical speciation, which was revealed to be Ag(0). A silver ion release investigation allowed for us to hypothesize that the L-Ag/MMT/beeswax coating could slow down biofilm formation while exerting mild antimicrobial action. The antibiofilm action was tested against the histamine-producing *Lentilactobacillus parabuchneri* bacterium. The developed coating is expected to inhibit biofilm formation. The IR-ATR flow analytical technique was used to monitor in situ the inhibition of the *L. parabuchneri* biofilm for 32 h, providing molecular insight into this phenomenon. The results indicate that the L-Ag/MMT/beeswax coating was able to slow down biofilm formation. This study indicated for the first time the in situ molecular changes of *L. parabuchneri* biofilm formation close to real time via flow FTIR-ATR spectroscopy under the influence of an L-Ag/MMT/beeswax coating. Furthermore,

OD measurements confirmed the antimicrobial activity of this coating. Last, the evaluation of the antibiofilm activity was supported with an SEM investigation on the bacteria incubated in contact with the antimicrobial coating.

**Supplementary Materials:** The following supporting information can be downloaded at: <https://www.mdpi.com/article/10.3390/antibiotics12020194/s1>. Figure S1: (a–c) TEM images and (d) histogram of L-AgNPs; Table S1: infrared vibrational band assignment of the *Lactobacillus parabuchneri* cell and biofilm functional groups; Figure S2: optical density (OD) measurement of *L. parabuchneri* bacterial suspension after 24 h incubation treated with L-Ag/MMT/beeswax, beeswax coatings, and without coating (bare silicon wafer). References [45,50,65,66,71–73] are cited in the supplementary materials.

**Author Contributions:** S.I.H.: performed most of the experiments, writing, review, and editing. D.B.: writing, review, and editing. S.I.H. and D.B.: performed the IR-ATR experiment. M.C.S.: performed TEM characterization, ETAAS investigation, and took part in manuscript revision. R.A.P.: XPS data treatment and interpretation, review, and editing. A.V. and A.A.: coordinated LASiS experiment and manuscript revision. C.G.: experimental discussion on LASiS technique and review. L.G.: took part in the scientific discussion, review, and editing. G.P.: took part in the scientific discussion, review, and editing. N.D.: performed XPS analyses, data treatment and interpretation, and revision. B.M.: coordinated IR-ATR study, review, and editing. N.C.: participated in scientific discussions, review, and editing, and supervised and coordinated the study. All authors have read and agreed to the published version of the manuscript.

**Funding:** This work is part of the Break Biofilms project, which has received funding from the European Union’s Horizon 2020 research and innovation program under the Marie Skłodowska Curie Grant agreement no. 813439. M.C.S. acknowledges the financial support from Fondo Sociale Europeo “Research for Innovation (REFIN)”; project no. 435A866B”. This research was supported by EU funding within the MUR PNRR Extended Partnership initiative on Emerging Infectious Diseases (project no. PE00000007, INF-ACT). N.C. acknowledges the partial financial support from Italian MIUR for National Project PON PROFOOD-IV (ARS01\_00755).

**Institutional Review Board Statement:** not applicable.

**Informed Consent Statement:** not applicable.

**Data Availability Statement:** not applicable.

**Acknowledgments:** The authors want to acknowledge Cinzia Di Franco at IFN–CNR (Istituto di Fotonica e Nanotecnologie–Consiglio Nazionale delle Ricerche), Sandra Ginger and the Focused Ion Beam Center at the Institute of Analytical and Bioanalytical Chemistry, and University of Ulm for the technical assistance with SEM imaging.

**Conflicts of Interest:** the authors declare no conflict of interest.

## References

1. Surveillance of Antimicrobial Resistance in Europe 2018. Available online: <https://www.ecdc.europa.eu/en/publications-data/surveillance-antimicrobial-resistance-europe-2018> (accessed on 24 March 2022).
2. Global Action Plan on Antimicrobial Resistance Available online: <https://apo.who.int/publications/i/item/global-action-plan-on-antimicrobial-resistance> (accessed on 6 February 2022).
3. Diaz, M.; Ladero, V.; Redruello, B.; Sanchez-Llana, E.; del Rio, B.; Fernandez, M.; Martin, M.C.; Alvarez, M.A. A PCR-DGGE Method for the Identification of Histamine-Producing Bacteria in Cheese. *Food Control* **2016**, *63*, 216–223. <https://doi.org/10.1016/j.foodcont.2015.11.035>.
4. Diaz, M.; del Rio, B.; Sanchez-Llana, E.; Ladero, V.; Redruello, B.; Fernández, M.; Martin, M.C.; Alvarez, M.A. Histamine-Producing *Lactobacillus parabuchneri* Strains Isolated from Grated Cheese Can Form Biofilms on Stainless Steel. *Food Microbiol.* **2016**, *59*, 85–91. <https://doi.org/10.1016/j.fm.2016.05.012>.
5. De A. Møller, C.O.; Castro-Mejía, J.L.; Krych, L.; Rattray, F.P. Histamine-Forming Ability of *Lentilactobacillus parabuchneri* in Reduced Salt Cheddar Cheese. *Food Microbiol.* **2021**, *98*, 103789. <https://doi.org/10.1016/j.fm.2021.103789>.
6. Bajrami, D.; Fischer, S.; Barth, H.; Hossain, S.I.; Cioffi, N.; Mizaikoff, B. Antimicrobial Efficiency of Chitosan and Its Methylated Derivative against *Lentilactobacillus Parabuchneri* Biofilms. *Molecules* **2022**, *27*, 8647. <https://doi.org/10.3390/molecules27248647>.
7. Muñoz-González, R.; Pino, C.; Henríquez, H.; Villanueva, F.; Riquelme, A.; Montealegre, R.; Agostini, D.; Batista-González, A.; Leiva, G.; Contreras, R.A. Elucidation of Antimicrobial and Antioxidant Activities of Selected Plant-Based Mayonnaise-Derived Essential Oils against Lactic Acid Bacteria. *J. Food Pro-Cessing Preserv.* **2022**, *46*, e16339. <https://doi.org/10.1111/jfpp.16339>.



8. Nguyen, N.D.; Nguyen, T.V.; Chu, A.D.; Tran, H.V.; Tran, L.T.; Huynh, C.D. A Label-Free Colorimetric Sensor Based on Silver Nanoparticles Directed to Hydrogen Peroxide and Glucose. *Arab. J. Chem.* **2018**, *11*, 1134–1143. <https://doi.org/10.1016/j.arabjc.2017.12.035>.
9. Campelo, J.M.; Luna, D.; Luque, R.; Marinas, J.M.; Romero, A.A. Sustainable Preparation of Supported Metal Nanoparticles and Their Applications in Catalysis. *ChemSusChem* **2009**, *2*, 18–45. <https://doi.org/10.1002/cssc.200800227>.
10. López-Lorente, A.I.; Picca, R.A.; Izquierdo, J.; Kranz, C.; Mizaikoff, B.; Di Franco, C.; Cárdenas, S.; Cioffi, N.; Palazzo, G.; Valentini, A. Ion Beam Sputtering Deposition of Silver Nanoparticles and TiO<sub>2</sub>/ZnO Nanocomposites for Use in Surface Enhanced Vibrational Spectroscopy (SERS and SEIRAS). *Microchim. Acta* **2018**, *185*, 153. <https://doi.org/10.1007/s00604-018-2708-7>.
11. Hossain, S.I.; Aziz, M.A.; Han, D.; Selvam, P.; Shanmugam, S. Fabrication of SPAEK–Cerium Zirconium Oxide Nanotube Composite Membrane with Outstanding Performance and Durability for Vanadium Redox Flow Batteries. *J. Mater. Chem. A* **2018**, *6*, 20205–20213. <https://doi.org/10.1039/C8TA08349E>.
12. Sportelli, M.C.; Izzi, M.; Volpe, A.; Clemente, M.; Picca, R.A.; Ancona, A.; Cioffi, N. Novel Polyethylene Oxide Coatings Implementing Ultra-Stable Laser-Ablated Silver Nanoparticles. *Appl. Surf. Sci.* **2020**, *507*, 145156. <https://doi.org/10.1016/j.apusc.2019.145156>.
13. Sun, G.; Jia, S.; Zhang, X.; Kang, Z.; Cui, M.; Wang, B.; Wang, B.; Yang, D.-P. Anchoring Core–Shell Cu@Cu<sub>2</sub>O Nanoparticles to Two-Dimensional Carbon Nanosheets for Bacterial Disinfection. *ACS Appl. Nano Mater.* **2021**, *4*, 9831–9841. <https://doi.org/10.1021/acsanm.1c02233>.
14. Terzioğlu, E.; Arslan, M.; Balaban, B.G.; Çakar, Z.P. Microbial Silver Resistance Mechanisms: Recent Developments. *World J. Microbiol. Biotechnol.* **2022**, *38*, 158.
15. Suchomel, P.; Kvittek, L.; Panacek, A.; Prucek, R.; Hrbac, J.; Vecerova, R.; Zboril, R. Comparative Study of Antimicrobial Activity of AgBr and Ag Nanoparticles (NPs). *PLoS ONE* **2015**, *10*, e0119202. <https://doi.org/10.1371/journal.pone.0119202>.
16. Kukushkina, E.A.; Hossain, S.I.; Sportelli, M.C.; Ditaranto, N.; Picca, R.A.; Cioffi, N. Ag-Based Synergistic Antimicrobial Composites. *A Crit. Review. Nanomater.* **2021**, *11*, 1687. [doi.org/10.3390/nano11071687](https://doi.org/10.3390/nano11071687).
17. Sportelli, M.C.; Picca, R.A.; Ronco, R.; Bonerba, E.; Tantillo, G.; Pollini, M.; Sannino, A.; Valentini, A.; Cataldi, T.R.I.; Cioffi, N. Investigation of Industrial Polyurethane Foams Modified with Antimicrobial Copper Nanoparticles. *Materials* **2016**, *9*, 544. <https://doi.org/10.3390/ma9070544>.
18. Makvandi, P.; Wang, C.; Zare, E.N.; Borzacchiello, A.; Niu, L.; Tay, F.R. Metal-Based Nanomaterials in Biomedical Applications: Antimicrobial Activity and Cytotoxicity Aspects. *Adv. Funct. Mater.* **2020**, *30*, 1910021. <https://doi.org/10.1002/adfm.201910021>.
19. Sportelli, M.C.; Clemente, M.; Izzi, M.; Volpe, A.; Ancona, A.; Picca, R.A.; Palazzo, G.; Cioffi, N. Exceptionally Stable Silver Nanoparticles Synthesized by Laser Ablation in Alcoholic Organic Solvent. *Colloids Surf. A: Physicochem. Eng. Asp.* **2018**, *559*, 148–158. <https://doi.org/10.1016/j.colsurfa.2018.09.046>.
20. Sportelli, M.C.; Izzi, M.; Volpe, A.; Clemente, M.; Picca, R.A.; Ancona, A.; Lugarà, P.M.; Palazzo, G.; Cioffi, N. The Pros and Cons of the Use of Laser Ablation Synthesis for the Production of Silver Nano-Antimicrobials. *Antibiotics* **2018**, *7*, 67. <https://doi.org/10.3390/antibiotics7030067>.
21. Dermatas, D.; Dadachov, M.S. Rietveld Quantification of Montmorillonites in Lead-Contaminated Soils. *Appl. Clay Sci.* **2003**, *23*, 245–255. [https://doi.org/10.1016/S0169-1317\(03\)00109-1](https://doi.org/10.1016/S0169-1317(03)00109-1).
22. Carretero, M.I. Clay Minerals and Their Beneficial Effects upon Human Health. A Review. *Appl. Clay Sci.* **2002**, *21*, 155–163. [https://doi.org/10.1016/S0169-1317\(01\)00085-0](https://doi.org/10.1016/S0169-1317(01)00085-0).
23. Özdemir, G.; Limoncu, M.H.; Yapar, S. The Antibacterial Effect of Heavy Metal and Cetylpridinium-Exchanged Montmorillonites. *Appl. Clay Sci.* **2010**, *48*, 319–323. <https://doi.org/10.1016/j.clay.2010.01.001>.
24. *Handbook of Clay Science*; Bergaya, F., Lagaly, G., Eds., Elsevier: Amsterdam, The Netherlands, 2013; ISBN 978-0-08-099371-3.
25. Tulloch, A.P. Beeswax—Composition and Analysis. *Bee World* **1980**, *61*, 47–62. <https://doi.org/10.1080/0005772X.1980.11097776>.
26. Pamplona-Zomenhan, L.C.; Pamplona, B.C.; da Silva, C.B.; Marcucci, M.C.; Mimica, L.M.J. Evaluation of the in vitro antimicrobial activity of an ethanol extract of Brazilian classified propolis on strains of *Staphylococcus aureus*. *Braz. J. Microbiol.* **2011**, *42*, 1259–1264. <https://doi.org/10.1590/S1517-83822011000400002>.
27. Fratini, F.; Cilia, G.; Turchi, B.; Felicioli, A. Beeswax: A Minireview of Its Antimicrobial Activity and Its Application in Medicine. *Asian Pac. J. Trop. Med.* **2016**, *9*, 839–843. <https://doi.org/10.1016/j.apjtm.2016.07.003>.
28. Fabra, M.J.; Talens, P.; Chiralt, A. Tensile Properties and Water Vapor Permeability of Sodium Caseinate Films Containing Oleic Acid–Beeswax Mixtures. *J. Food Eng.* **2008**, *85*, 393–400. <https://doi.org/10.1016/j.jfoodeng.2007.07.022>.
29. Jafari, S.M.; Khanzadi, M.; Mirzaei, H.; Dehnad, D.; Chegini, F.K.; Maghsoudlou, Y. Hydrophobicity, Thermal and Micro-Structural Properties of Whey Protein Concentrate–Pullulan–Beeswax Films. *Int. J. Biol. Macromol.* **2015**, *80*, 506–511. <https://doi.org/10.1016/j.ijbiomac.2015.07.017>.
30. Stenclova, P.; Freisinger, S.; Barth, H.; Kromka, A.; Mizaikoff, B. Cyclic Changes in the Amide Bands Within *Escherichia Coli* Biofilms Monitored Using Real-Time Infrared Attenuated Total Reflection Spectroscopy (IR-ATR). *Appl. Spectrosc* **2019**, *73*, 424–432. <https://doi.org/10.1177/0003702819829081>.
31. Anicuta, S.G.; Dobre, L.; Stroescu, M.; Jipa, I. Fourier Transform Infrared (FTIR) Spectroscopy for Characterization of Antimicrobial Films Containing Chitosan. *Analele Universității din Oradea, Fascicula: Ecotoxicologie, Zootehnie și Tehnologii de Industrie Alimentară* **2010**, pp. 815–822. Available online: <https://www.cabdirect.org/cabdirect/abstract/20113173121> (accessed on 31 December 2022).

32. Sportelli, M.C.; Kranz, C.; Mizaikoff, B.; Cioffi, N. Recent Advances on the Spectroscopic Characterization of Microbial Biofilms: A Critical Review. *Anal. Chim. Acta* **2022**, *1195*, 339433. <https://doi.org/10.1016/j.aca.2022.339433>.
33. Lorite, G.S.; de Souza, A.A.; Neubauer, D.; Mizaikoff, B.; Kranz, C.; Cotta, M.A. On the Role of Extracellular Polymeric Substances during Early Stages of *Xylella Fastidiosa* Biofilm Formation. *Colloids Surf. B: Biointerfaces* **2013**, *102*, 519–525. <https://doi.org/10.1016/j.colsurfb.2012.08.027>.
34. Bazán, J.C.; García, N.J.; Dristas, J.A.; Spetter, C.V. Ionic Conductivity in Montmorillonite-Doped Silver Iodide. *Solid State Ion.* **2004**, *170*, 57–61. [https://doi.org/10.1016/S0167-2738\(03\)00031-6](https://doi.org/10.1016/S0167-2738(03)00031-6).
35. Giovannini, G.; Garoli, D.; Rupper, P.; Neels, A.; Rossi, R.M.; Boesel, L.F. Metal-Modified Montmorillonite as Plasmonic Microstructure for Direct Protein Detection. *Sensors* **2021**, *21*, 2655. <https://doi.org/10.3390/s21082655>.
36. Xu, G.; Tazawa, M.; Jin, P.; Nakao, S.; Yoshimura, K. Wavelength Tuning of Surface Plasmon Resonance Using Dielectric Layers on Silver Island Films. *Appl. Phys. Lett.* **2003**, *82*, 3811–3813. <https://doi.org/10.1063/1.1578518>.
37. Beck, F.J.; Polman, A.; Catchpole, K.R. Tunable Light Trapping for Solar Cells Using Localized Surface Plasmons. *J. Appl. Phys.* **2009**, *105*, 114310. <https://doi.org/10.1063/1.3140609>.
38. Jeong, S.-H.; Choi, H.; Kim, J.Y.; Lee, T.-W. Silver-Based Nanoparticles for Surface Plasmon Resonance in Organic Optoelectronics. *Part. Part. Syst. Charact.* **2015**, *32*, 164–175. <https://doi.org/10.1002/ppsc.201400117>.
39. Bera, S.; Gangopadhyay, P.; Nair, K.G.M.; Panigrahi, B.K.; Narasimhan, S.V. Electron Spectroscopic Analysis of Silver Nanoparticles in a Soda-Glass Matrix. *J. Electron. Spectrosc. Relat. Phenom.* **2006**, *152*, 91–95. <https://doi.org/10.1016/j.elspec.2006.03.008>.
40. Paladini, F.; Picca, R.A.; Sportelli, M.C.; Cioffi, N.; Sannino, A.; Pollini, M. Surface Chemical and Biological Characterization of Flax Fabrics Modified with Silver Nanoparticles for Biomedical Applications. *Mater. Sci. Eng. C* **2015**, *52*, 1–10. <https://doi.org/10.1016/j.msec.2015.03.035>.
41. Coughlan, L.M.; Cotter, P.D.; Hill, C.; Alvarez-Ordóñez, A. New Weapons to Fight Old Enemies: Novel Strategies for the (Bio)Control of Bacterial Biofilms in the Food Industry. *Front. Microbiol.* **2016**, *7*, 1641.
42. Qing, Y.; Cheng, L.; Li, R.; Liu, G.; Zhang, Y.; Tang, X.; Wang, J.; Liu, H.; Qin, Y. Potential Antibacterial Mechanism of Silver Nanoparticles and the Optimization of Orthopedic Implants by Advanced Modification Technologies. *Int. J. Nanomed.* **2018**, *13*, 3311–3327. <https://doi.org/10.2147/IJN.S165125>.
43. Yun, H.; Kim, J.D.; Choi, H.C.; Lee, C.W. Antibacterial Activity of CNT-Ag and GO-Ag Nanocomposites Against Gram-Negative and Gram-Positive Bacteria. *Bull. Korean Chem. Soc.* **2013**, *34*, 3261–3264. <https://doi.org/10.5012/bkcs.2013.34.11.3261>.
44. Ediriweera, E.R.H.S.; Premarathna, N.Y. Medicinal and Cosmetic Uses of Bee’s Honey—A Review. *AYU* **2012**, *33*, 178–182. <https://doi.org/10.4103/0974-8520.105233>.
45. Ojeda, J.J.; Romero-Gonzalez, M.E.; Pouran, H.M.; Banwart, S.A. In Situ Monitoring of the Biofilm Formation of *Pseudomonas Putida* on Hematite Using Flow-Cell ATR-FTIR Spectroscopy to Investigate the Formation of Inner-Sphere Bonds between the Bacteria and the Mineral. *Mineral. Mag.* **2008**, *72*, 101–106. <https://doi.org/10.1180/minmag.2008.072.1.101>.
46. Pousti, M.; Joly, M.; Roberge, P.; Amirdehi, M.A.; Bégin-Drolet, A.; Greener, J. Linear Scanning ATR-FTIR for Chemical Mapping and High-Throughput Studies of *Pseudomonas* Sp. *Anal. Chem.* **2018**, *90*, 14475–14483. <https://doi.org/10.1021/acs.analchem.8b04279>.
47. Humbert, F.; Quilès, F. *In-Situ Study of Early Stages of Biofilm Formation under Different Environmental Stresses by ATR-FTIR Spectroscopy. Science against Microbial Pathogens: Communicating Current Research and Technological Advances*; Mendez-Vilas, A., Ed. HAL Open Science, Formatex Research Center: Badajoz, Spain, 2011; pp. 889–895.
48. Maquelin, K.; Kirschner, C.; Choo-Smith, L.; van den Braak, N.; Endtz, H.P.; Naumann, D.; Puppels, G. Identification of medically relevant microorganisms by vibrational spectroscopy. *J. Microbiol. Methods* **2002**, *51*, 255–271. [https://doi.org/10.1016/S0167-7012\(02\)00127-6](https://doi.org/10.1016/S0167-7012(02)00127-6).
49. Yunda, E.; Alem, H.; Francius, G.; Gago, R.; Quilès, F. Chemical Functionalization of the Zinc Selenide Surface and Its Impact on *Lactobacillus Rhamnosus* GG Biofilms. *ACS Appl. Mater. Interfaces* **2020**, *12*, 14933–14945. <https://doi.org/10.1021/acsami.0c01335>.
50. Oust, A.; Møretør, T.; Kirschner, C.; Narvhus, J.A.; Kohler, A. FT-IR Spectroscopy for Identification of Closely Related Lactobacilli. *J. Microbiol. Methods* **2004**, *59*, 149–162. <https://doi.org/10.1016/j.mimet.2004.06.011>.
51. Kudrinskiy, A.A.; Ivanov, A.Y.; Kulakovskaya, E.V.; Klimov, A.I.; Zherebin, P.M.; Khodarev, D.V.; Le, A.-T.; Tam, L.T.; Lisichkin, G.V.; Krutyakov, Y.A. The Mode of Action of Silver and Silver Halides Nanoparticles against *Saccharomyces Cerevisiae* Cells. *J. Nanoparticles* **2014**, *2014*, 568635. <https://doi.org/10.1155/2014/568635>.
52. Ascone, P.; Maurer, J.; Haldemann, J.; Irmeler, S.; Berthoud, H.; Portmann, R.; Fröhlich-Wyder, M.T.; Wechsler, D. Prevalence and Diversity of Histamine-Forming *Lactobacillus Parabuchneri* Strains in Raw Milk and Cheese—A Case Study. *Int. Dairy J.* **2017**, *70*, 26–33. <https://doi.org/10.1016/j.idairyj.2016.11.012>.
53. Fröhlich-Wyder, M.T.; Guggisberg, D.; Badertscher, R.; Wechsler, D.; Wittwer, A.; Irmeler, S. The Effect of *Lactobacillus Buchneri* and *Lactobacillus Parabuchneri* on the Eye Formation of Semi-Hard Cheese. *Int. Dairy J.* **2013**, *33*, 120–128. <https://doi.org/10.1016/j.idairyj.2013.03.004>.
54. Bodmer, S.; Imark, C.; Kneubühl, M. Biogenic Amines in Foods: Histamine and Food Processing. *Inflamm. Res.* **1999**, *48*, 296–300. <https://doi.org/10.1007/s000110050463>.
55. Dinić, M.; Pecikoza, U.; Djokić, J.; Stepanović-Petrović, R.; Milenković, M.; Stevanović, M.; Filipović, N.; Begović, J.; Golić, N.; Lukić, J. Exopolysaccharide Produced by Probiotic Strain *Lactobacillus Paraplantarum* BCGG11 Reduces Inflammatory Hyperalgesia in Rats. *Front. Pharmacol.* **2018**, *9*, 1. <https://doi.org/10.3389/fphar.2018.00001>.

56. Cai, S.; Singh, B.R. A Distinct Utility of the Amide III Infrared Band for Secondary Structure Estimation of Aqueous Protein Solutions Using Partial Least Squares Methods. *Biochemistry* **2004**, *43*, 2541–2549. <https://doi.org/10.1021/bi030149y>.
57. Sheng, G.P.; Yu, H.Q.; Li, X.Y. Extracellular Polymeric Substances (EPS) of Microbial Aggregates in Biological Wastewater Treatment Systems: A Review. *Biotechnol. Adv.* **2010**, *28*, 882–894. <https://doi.org/10.1016/j.biotechadv.2010.08.001>.
58. Flemming, H.C.; Wingender, J. The Biofilm Matrix. *Nat. Rev. Microbiol.* **2010**, *8*, 623–633.
59. Sutherland, I.W. The Biofilm Matrix—An Immobilized but Dynamic Microbial Environment. *Trends Microbiol.* **2001**, *9*, 222–227. [https://doi.org/10.1016/S0966-842X\(01\)02012-1](https://doi.org/10.1016/S0966-842X(01)02012-1).
60. Chao, Y.; Zhang, T. Surface-Enhanced Raman Scattering (SERS) Revealing Chemical Variation during Biofilm Formation: From Initial Attachment to Mature Biofilm. *Anal. Bioanal. Chem.* **2012**, *404*, 1465–1475. <https://doi.org/10.1007/s00216-012-6225-y>.
61. Pink, J.; Smith-Palmer, T.; Chisholm, D.; Beveridge, T.J.; Pink, D.A. An FTIR Study of *Pseudomonas Aeruginosa* PAO1 Biofilm Development: Interpretation of ATR-FTIR Data in the 1500–1180  $\text{cm}^{-1}$  Region. *Biofilms* **2005**, *2*, 165–175. <https://doi.org/10.1017/S14790505001936>.
62. Badireddy, A.R.; Farner Budariz, J.; Marinakos, S.M.; Chellam, S.; Wiesner, M.R. Formation of Silver Nanoparticles in Visible Light-Illuminated Waters: Mechanism and Possible Impacts on the Persistence of AgNPs and Bacterial Lysis. *Environ. Eng. Sci.* **2014**, *31*, 338–349. <https://doi.org/10.1089/ees.2013.0366>.
63. Fahs, A.; Quilès, F.; Jamal, D.; Humbert, F.; Francius, G. In Situ Analysis of Bacterial Extracellular Polymeric Substances from a *Pseudomonas Fluorescens* Biofilm by Combined Vibrational and Single Molecule Force Spectroscopies. *J. Phys. Chem. B* **2014**, *118*, 6702–6713. <https://doi.org/10.1021/jp5030872>.
64. Caniglia, G.; Sportelli, M.C.; Heinzmann, A.; Picca, R.A.; Valentini, A.; Barth, H.; Mizaikoff, B.; Cioffi, N.; Kranz, C. Silver-Fluoropolymer (Ag-CFX) Films: Kinetic Study of Silver Release, and Spectroscopic-Microscopic Insight into the Inhibition of *P. Fluorescens* Biofilm Formation. *Anal. Chim. Acta* **2022**, *1212*, 339892. <https://doi.org/10.1016/j.aca.2022.339892>.
65. Ojeda, J.J.; Dittrich, M. Fourier Transform Infrared Spectroscopy for Molecular Analysis of Microbial Cells. *Methods Mol. Biol.* **2012**, *881*, 187–211. [https://doi.org/10.1007/978-1-61779-827-6\\_8](https://doi.org/10.1007/978-1-61779-827-6_8).
66. Schmitt, J.; Fringeli, U.P.; Flemming, H.-C. Structural and Temporal Behavior of Biofilms Investigated by FTIR-ATR Spectroscopy. *AIP Conf. Proc.* **1998**, *430*, 312. <https://doi.org/10.1063/1.55788>.
67. Lorite, G.S.; Janissen, R.; Clerici, J.H.; Rodrigues, C.M.; Tomaz, J.P.; Mizaikoff, B.; Kranz, C.; de Souza, A.A.; Cotta, M.A. Surface Physicochemical Properties at the Micro and Nano Length Scales: Role on Bacterial Adhesion and *Xylella Fastidiosa* Biofilm Development. *PLoS ONE* **2013**, *8*, e75247. <https://doi.org/10.1371/journal.pone.0075247>.
68. Wang, H.; Ding, S.; Wang, G.; Xu, X.; Zhou, G. In Situ Characterization and Analysis of *Salmonella* Biofilm Formation under Meat Processing Environments Using a Combined Microscopic and Spectroscopic Approach. *Int. J. Food Microbiol.* **2013**, *167*, 293–302. <https://doi.org/10.1016/j.ijfoodmicro.2013.10.005>.
69. Dobbs, G.T.; Mizaikoff, B. Shining New Light on Old Principles: Localization of Evanescent Field Interactions at Infrared-Attenuated Total Reflection Sensing Interfaces. *Appl. Spectrosc.* **2006**, *60*, 573–583. <https://doi.org/10.1366/000370206777670585>.
70. Bajrami, D.; Fischer, S.; Barth, H.; Sarquis, M.A.; Ladero, V.M.; Fernández, M.; Sportelli, M.C.; Cioffi, N.; Kranz, C.; Mizaikoff, B. In Situ Monitoring of *Lentilactobacillus Parabuchneri* Biofilm Formation via Real-Time Infrared Spectroscopy. *npj Biofilms Microbiomes* **2022**, *8*, 92. <https://doi.org/10.1038/s41522-022-00353-5>.
71. Sharma, G.; Prakash, A. Combined Use of Fourier Transform Infrared and Raman Spectroscopy To Study Planktonic and Biofilm Cells of *Cronobacter Sakazakii*. *J. Microbiol. Biotechnol. Food Sci.* **2014**, *9*, 310–314.
72. Sportelli, M.C.; Tütüncü, E.; Picca, R.A.; Valentini, M.; Valentini, A.; Kranz, C.; Mizaikoff, B.; Barth, H.; Cioffi, N. Inhibiting *P. fluorescens* Biofilms with Fluoropolymer-Embedded Silver Nanoparticles: An in-Situ Spectroscopic Study. *Sci. Rep.* **2017**, *7*, <https://doi.org/10.1038/s41598-017-12088-x>.
73. McWhirter, M.J.; Bremer, P.J.; McQuillan, A.J. Direct Infrared Spectroscopic Evidence of PH- and Ionic Strength-Induced Changes in Distance of Attached *Pseudomonas Aeruginosa* from ZnSe Surfaces. *Langmuir* **2002**, *18*, 1904–1907. <https://doi.org/10.1021/la010928k>.

**Disclaimer/Publisher’s Note:** The statements, opinions and data contained in all publications are solely those of the individual author(s) and contributor(s) and not of MDPI and/or the editor(s). MDPI and/or the editor(s) disclaim responsibility for any injury to people or property resulting from any ideas, methods, instructions or products referred to in the content.